Theses and Dissertations

Spring 2013

A new algorithm for cortical bone segmentation with its validation and applications to in vivo imaging

Cheng Li
University of Iowa

A NEW ALGORITHM FOR CORTICAL BONE SEGMENTATION WITH ITS

VALIDATION AND APPLICATIONS TO IN VIVO IMAGING

by

Cheng Li

A thesis submitted in partial fulfillment
of the requirements for the Master of
Science degree in Electrical and Computer Engineering
in the Graduate College of
The University of Iowa

May 2013

Thesis Supervisor: Associate Professor Punam K. Saha

Graduate College
The University of Iowa
Iowa City, Iowa

CERTIFICATE OF APPROVAL

_____

MASTER'S THESIS

_____

This is to certify that the Master's thesis of

Cheng Li

has been approved by the Examining Committee
for the thesis requirement for the Master of Science
degree in Electrical and Computer Engineering at the May 2013 graduation.

Thesis Committee: _____
                  Punam K. Saha, Thesis Supervisor

                  _____
                  Xiaodong Wu

                  _____
                  Mona Garvin

ACKNOWLEDGMENTS

ABSTRACT

Cortical bone is an osseous tissue forming the cortex in our skeleton that supports and protects skeletal functions. Cortical bone segmentation is usually the first step for quantitative cortical bone imaging research. Quality of cortical bone segmentation is one of the most critical factor in determining effectiveness and usefulness of cortical bone measures in a bone imaging study aimed at understanding disease effects, fracture risk and or interventional outcomes. Previous methods primarily focus on local image features and ignore ad therefore fail to utilize larger geometric and topologic contextual knowledge into the segmentation algorithm. Such methods often results in compromised performance under *in vivo* imaging conditions suffering from low signal to noise ratio and low spatial resolution leaving significant partial volume effects. This thesis presents a new cortical bone segmentation method that utilizes larger contextual and topologic knowledge of distal tibia bone through fuzzy distance transform and connectivity analyses. The input of the method is one threshold and other steps are automatic. An accuracy of 95.1% in terms of percent of volume agreement with gold standard segmentation results and a repeat MD-CT scan intra-class correlation of 98.0% were observed on a cadaveric study. An in vivo study involving sixteen age and body mass index order matched pairs of male and female volunteers has shown that male subjects on average have 16.3% thicker cortex and 4.7% increased porosity as compared to females, and athletes have 3.9% less porosity as compared to control group.

TABLE OF CONTENTS

LIST OF FIGURES

CHAPTER ONE

INTRODUCTION

1.1 Cortical Bone Analysis in Clinical Practice

Cortical bone, which forms the cortex of the bone, is one of the two types of osseous tissue that form bones. Adult bone diseases, especially osteoporosis, lead to increased risk of fracture associated with substantial morbidity, mortality, and financial costs [1][2][3]. Clinically, osteoporosis is defined by low bone mineral density (BMD). BMD only explains about 65-75% of the variance in bone strength [4][5], while the remaining variance is due to the cumulative and synergistic effects of various factors, including bone macro- and micro-architecture, tissue composition, and micro-damage [6][7]. For this reason, currently, much interest exists in the study of other factors affecting bone strength including cortical and trabecular bone micro- and macro-architecture [7][8]. Several studies have reported that, along with trabecular bone micro-architecture, structural changes in cortical bone add information to BMD in assessing bone strength and discriminating between healthy individuals and patients with osteoporotic fractures [1][9][10][11][12][13][14][15]. Fracture risk, one of the serious consequences of osteoporosis, is also influenced by alterations in bone morphology, such as the distribution of bone mass between cortical and trabecular bone, cortical thickness and porosity [2][3]. Cortical bone loss and periosteal new bone formation are also used for therapeutic evaluation of osteoarthritis [4].

Over the last few decades, several studies have been reported toward understanding the role of cortical bone properties in determining the status of bone health and treatment effects. Cortical bone properties, such as bone mineral density (BMD) and thickness, have been proved to be highly related to bone turnover under bone diseases such as osteoporosis [5][6]. There are several studies aiming at alterations of bone

morphology including cortical bone in specific groups of people differed by age, gender or region [6][8][9] and to determine discriminatory cortical bone data under therapy, especially for postmenopausal women who are at high risk of osteoporosis and low trauma fractures. Cortical BMD, thickness and microstructure are effective indicators of different pharmaceutical intervention, such as Denosumab, Alendronate and Teriparatide [10][11]. It has been demonstrated that cortical bone bears the bulk of axial loads in the distal radius and tibia [13] and the load distribution is an important factor in the determining of bone strength and fracture risk [14][15]. Also, research studies have established the relation between cortical bone porosity and bone biomechanical strength [16]. These results and observations in a large number of clinical and research studies demonstrate the importance of cortical bone parameters in in understanding overall bone quality.

1.2 Bone Imaging and Previous Segmentation Study

In this paper, we develop a new method for segmenting cortical bone via in vivo Multi-Detector Computed Tomography (MD-CT) imaging. MD-CT imaging in clinical applications has shown enormous power in clinical diagnose. MD-CT scanners have progressively increased the number of detectors and reduced scan acquisition times. Micro-CT has almost the most powerful ability for imaging bone structure, since it can offer nominal isotropic resolution as low as 10 μm. Although Micro-CT scanners are hard scan large object such as part of living human, it can be used for human biopsies [20]. Major benefits of HR MD-CT have been widely utilized nowadays, including: (1) short MD-CT scan time reduces motion artifacts; (2) better patient comfort with MD-CT scanners; (3) large FOV along with model-based registration methods for subject-specific region-of-interest (ROI) selection reduces positioning error. Also, MD-CT offers the opportunity to assess bone quality at central sites using a higher radiation dose.

Previous cortical bone studies are mainly conducted using Micro-CT [21][22] or HR-pQCT [5][6][14]. MD-CT cortical bone studies are few. Due to the high resolution, Micro-CT structure analysis can also be used as a golden standard. Laib A. et al [23] proposed a semi-automated slice-by-slice hand contouring method on 3D-QCT images, which is pretty precise that it was once the gold standard for cortical bone segmentation, but is very effort-costing. Gelaude F. et al. [25] implemented methods using region growing, energy minimizing spline curves, and deformable model to enhance result and improve consistency on CT data, but are complex and remain semi-automated. Gomberg B. R. [26] et al. developed a method which estimates marrow density range first, then uses region growing inside such range followed by opening operation, and applied on Magnetic Resonance Images (MRI). Buie H. R. [22]et al. proposed an automatic duel threshold method based on threshold and connective filter on Micro-CT data, which can get good result. But this algorithm is designed and verified on Micro-CT images, and is sensitive to noise so not easy to be applied on low-quality CT images. Valentinitsch A. et al. developed a machine learning method on HR-pQCT data, which train a set of bone images which is manually labeled cortical structure to generate classier which use the local property of each voxel as input [27]. This method can have good segmentation, but that highly depends on training process. Treece G. et al. [28] used image's inplane point spread function to calculate femur cortex thickness, and improved his method in [29] by assuming a specific, fixed value for the density. But besides calculating cortical measures, those methods do not provide complete segment mask, especially considering their use of blurred image.

In this paper, a new cortical bone segmentation method based on fuzzy topology is proposed. It uses fuzzy connectivity and fuzzy distance transform to find the periosteum of the bone, then uses fuzzy distance transform to find the endosteum. This method is fully automated, which only needs a threshold as input. The method will be proved to be able to get good result on MD-CT data for getting cortical bone thickness

and BMD, where accuracy, reproducibility and effectiveness will be verified. To verify accuracy, MD-CT images of 10 cadaveric tibia specimens are processed, and manual drawing by independent expert on certain slices of each data will provide ground truth of segmentation, which will compare with our segmentation result to compute overlap and error of cortical measures. To verify reproducibility, twenty-four cadaveric tibia specimens have been scanned for three times with different position, and after processing, ICC of cortical measures will be done inside the three scans. To verify the effectiveness, cortical measures will be applied on forty-five pairs of height matched male and female tibia, 10 pairs of height matched athletes and control group, ten pairs of height matched athlete and control group, and pair t-test will be conduct on cortical measures.

1.3 Outline

This thesis will show the work about the fuzzy topology based cortical bone segmentation method in detail. In Chapter 2, we discuss the theory of fuzzy connectedness and fuzzy distance transform. In Chapter 3, we show in detail how the method works, and the details how experiments will be conducted. In Chapter 4, we present the quantity result of the experiment and analysis consisting of accuracy, reproducibility and applicability.

CHAPTER TWO

BACKGROUND THEORY

In this section, we will introduce basic theories used in this thesis, and give some definitions of mathematic notations.

The method proposed in this thesis is mainly based on fuzzy connectedness and fuzzy distance transform. These are both common applications of fuzzy logic. Fuzzy logic is a form of probabilistic logic. Images produced by any imaging device are always disturbed by noise, uneven illumination, limited spatial resolution, partial occlusions, etc. In such images, it is hard to do image analysis based on crisp (or hard-coded) relationships between or within the individual regions to be segmented. Fuzzy logic takes the uncertainties into consideration, which rather than defining crisp relations, attempts to describe the image processing task with fuzzy rules such as if two regions have about the same gray-value and if they are relatively close to each other in space, then they likely belong to the same object [32]. In contrast with traditional logic which uses binary sets where there is only two-value logic, true or false, fuzzy logic variables are usually extended to handle the concept of partial truth, which indicates the probability of the truth.

2.1 Fuzzy Connectedness

Fuzzy connectedness [28] segmentation is attempting to perform the segmentation by considering the likelihood of whether nearby image elements belong together. If they seem to belong to the same object based on their image and spatial properties, they are assigned to the same region. In other words, it focuses on hanging togetherness property which is then described using fuzzy logic.

MD-CT images are represented in three-dimensional (3-D) rectangular grids denoted by Z^3 and a digital CT image may be expressed by a function $f_{CT}: Z^3 \rightarrow$

$[\min_{CT}, \max_{CT}]$. Each grid point $p \in Z^3$ is referred to as a *voxel* whose size is defined by image resolution. Two voxels $p = (p_1, p_2, p_3), q = (q_1, q_2, q_3) \in Z^3$ are 26-adjacent if and only if, $\forall i \in \{1,2,3\}, |p_i - q_i| \leq 1$; p, q are referred to as 6-adjacent if and only if $\max_i |p_i - q_i| \leq 1$. The set of all 26-adjacent voxels of p including itself is denoted as $N(p)$. In any sub-region C of Z^3, a nonempty path p_{cd} in C from c to d is a sequence $\{c = c_1, c_2, \ldots, c_l = d\}$ of $l \geq 1$ voxels in C, in which any successive two voxels are 26-adjacent. The set of all paths in C from c to d is denoted by P_{cd}. The set of all paths in C is denoted by P_C.

Let C = (C,f) be any scene over (Z^3, α), where f denotes voxel intensity. A fuzzy relation α in C is said to make $\mu_\alpha(c,d)$ be a fuzzy adjacency if it is a non-increasing function of the distance $\|c-d\|$ between c and d. It is usually assigned 0 when c and d are not 26-adjancent. Any fuzzy relation κ in is said to be a fuzzy affinity in C if it is reflexive and symmetric, and proportional to fuzzy adjacency. In common practical segmentation usage, for any c, d $\in$ C, $\mu_\kappa(c,d)$ is usually $\mu_\alpha(c,d)$ times one of the following: 1) one; 2) the homogeneity of the voxel intensities at c and d; 3) the closeness of the voxel intensities [31]. For all paths $p_{cd} \in P_C$, assign a strength μ_N assigned to each path, as the smallest fuzzy affinity value between any two successive voxels on the path, i.e., $\mu_N(p_{cd}) = \min_{1 \leq i \leq l_p} [\mu_\kappa(c_{i-1}, c_i)]$.

Fuzzy κ-connectedness $\mu_K(c,d)$ between c and d in C is defined as the largest path strength of all path p_{cd} in P_{cd}. i.e., for any c, d $\in$ C, $\mu_K(c,d) = \max_{p \in P_{cd}} \mu_N(p)$, or:

$$\mu_K(c,d) = \max_{p \in P_{cd}} \left[\min_{1 \leq i \leq l_p} [\mu_\kappa(c_{i-1}, c_i)] \right]$$

where p is the path $\{c_1, c_2, \ldots, c_{lp}\}$.

Using dynamic algorithm can compute the fuzzy connectedness value. Based on this definition of connectedness, some derivative new kinds of fuzzy connectedness, such as relative fuzzy connectivity [32], scale-based fuzzy connectivity [34] and iterative relative fuzzy connectedness [35] are designed. Many applications, such as fuzzy object

extraction [28] and fuzzy connectivity segmentation [31], are proposed. Here we will not discuss about those.

2.2 Fuzzy Distance Transform

Fuzzy Distance Transform (FDT) [36] is a enhancement of distance transform (DT) on fuzzy objects. Comparing with DT, FDT usually can get better result in many imaging applications especially medical images, since there are often situations with data inaccuracies, graded object compositions, or limited image resolution.

We use same definitions of space, voxel, adjacency, path, etc. as discussed in Fuzzy Connectness part. The cortical bone segmentation algorithm presented here utilizes the fuzzy distance transform (FDT) [12]. A fuzzy object $\mathcal{O}$ is a fuzzy subset $\{(p, f_O(p)) \mid p \in Z^3\}$ where f_O is its membership function. FDT computes the distance of a candidate voxel inside the support $O = \{p \mid p \in Z^3 \wedge f_O(p) > 0\}$ of a fuzzy object $\mathcal{O}$ from its background $B = Z^3 - O$. The first step during FDT computation is an initialization with the zero FDT value inside B and a large value inside the support O. The second step is an iterative propagation of FDT values using the following equation:

$$FDT_O(p) = \min_{q \in N(p)} FDT(q) + \tfrac{1}{2}\big(f_O(p) + f_O(q)\big)|p - q|.$$

It may be noted that the FDT value at any voxel p is monotonically non-increasing during the propagation step. Here, we introduce some simple variations in the FDT algorithm and demonstrate its utility in the current application. Specifically, three sets are defined – (1) L: set of voxels initialized with a large value, (2) U: set of voxels initialized with non-large values, and (3) V: the set of voxels where no path propagation is allowed. Also, the value of initialization at each voxel inside U may be non-zero as well as non-uniform.

CHAPTER THREE

METHODS AND EXPERIMENTAL SETTING

In this section, we describe the new cortical bone segmentation algorithm for in vivo MD-CT imaging of distal tibia along with experimental plans and methods evaluating the performance and effectiveness of the algorithm.

3.1 Bone Alignment and ROI Detection

The cortical bone segmentation method is initiated with a preprocessing module which produces an axial cylindrical region of interest (ROI) taken from the same anatomic location of individual's bone. This module begins with conversion of CT image values into bone mineral density (BMD) values using a calibration phantom which is scanned every time a phantom or a human subject is scanned. All subsequent operations are performed on BMD images.

Here we establish our threshold on BMD at a value of 1180mg/cc. The BMD threshold value was set as the average of manually selected thresholds by three users on five randomly selected *in vivo* MD-CT data sets where each user was asked to select a threshold to isolate bone from marrow.

The next step of cortical bone segmentation algorithm is to separate the tibial region from other bones and soft tissues. This step is accomplished firstly by using this threshold and then isolating tibial region as the largest 26-component in the thresholded image as shown in Figure 1(b).
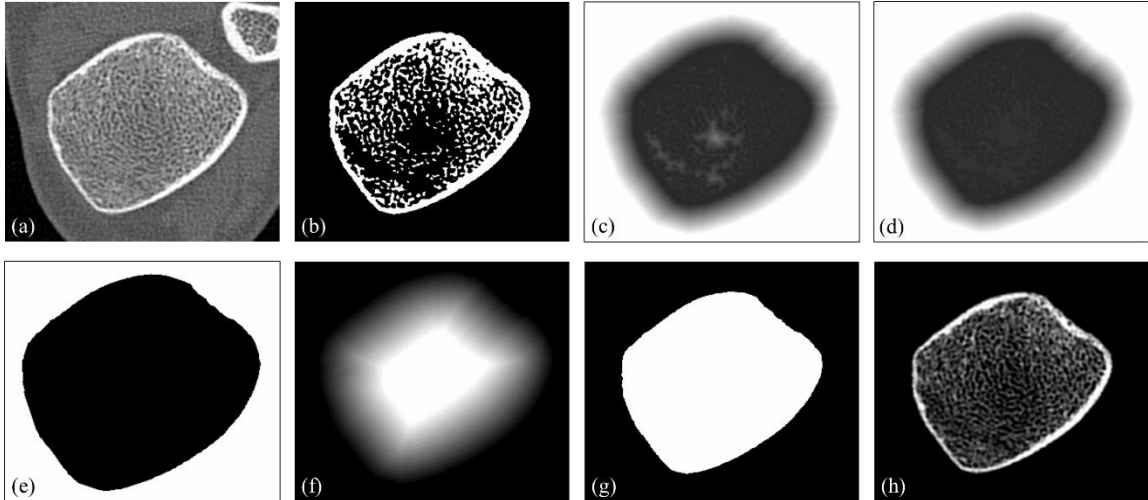
Figure 1   Results of intermediate steps of filling bone process. (a) BMD image. (b) The largest component. (c) Compute DT from bone voexls. (d) Compute fuzzy connectivity. (e) Threshold the fuzzy connectivity result. (f) Compute DT from surrounding region. (g) Filled bone region. (h) Tibia region bounded by filled bone.

We define the fuzzy affinity as:

$$\mu_\kappa(c,d) = \begin{cases} \min\big(f(c), f(d)\big), & \text{if } c, d \text{ are } 26 - adjacent \\ 0, & \text{otherwise} \end{cases},$$

and a filled-in bone shape is generated using the following steps:

Step 1: Compute distance transform (DT) at background voxels from bone voxels (Figure 1(c)).

Step 2: Compute fuzzy connectivity of the DT map with the eight corner image voxels as seeds (Figure 1(d)). Ideally, background voxels inside the tibial cavity should be disconnected from the eight corner seed voxels. Even if there are small leaks on tibial cortex and fuzzy connectivity paths may sneak through them, the fuzzy connectivity at tibial cavity is small due to small size of leaks. So fuzzy connectivity values are much lower inside the tibia region.

Step 3: Apply a DT connectivity threshold thr on fuzzy connectivity image, which will isolate the tibial region as well as a surrounding band with width thr (Figure 1(e)). Use S_{thr} to denote this region.

Step 4: Compute DT from S_{thr} (Figure 1(f)) and select the region thresholded at thr.

Then we get a filled tibia bone region on the result binary image, as shown in Figure 1(g). This filled bone region can be used to remove the fibula and tissue in future steps, as Figure 1(h), in order to limit the region of interest into only the tibia region.

This filled-in bone (Figure 2(b)) is used to reorient the tibia and to identify the distal tibial end plateau defined as the most proximal location on the distal tibial endplate. First, a rough estimate of the distal tibial plateau location is performed by analyzing the cross sectional images of filled-in bone. The distal tibial plateau is located just above the first image slice containing a cavity in the filled-in bone while tracing proximal-to-distal. In general, such a 2-D cavity consists of multiple voxels; therefore, the center of gravity of the cavity is used as the location of the distal tibial plateau (Figure 2(c)). Image slices above 8% of tibial length from the end plateau are used to compute the tibial axis; see Figure 2(c). The axis of tibia is computed as the best fit line to the 40% peeled region of tibia as shown in Figure 2(c). The bone is reoriented to align its axis with the image z-axis (Figure 2(d)). At the time of reorientation, the bone is simultaneously interpolated at 150 micron isotropic voxel and the distal tibial end plateau is relocated. Four adjacent axial cylindrical ROIs, each covering 2% of the tibial length, is located at 8%, 10%, 12% and 14% proximal to the distal endplate as shown in Figure 2(d). All cortical bone segmentation and analyses was applied over this axial cylindrical ROI covering 8% of the tibial length. The tibial length was determined by locating distal and proximal tibial plateaus in MD-CT scout scans.
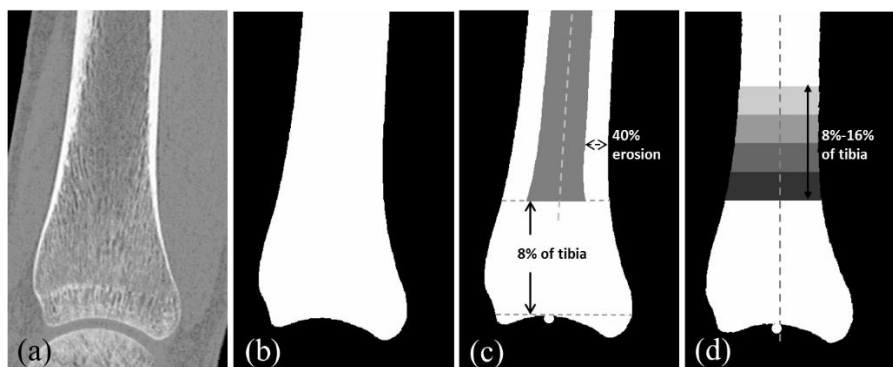
Figure 2   Illustration of the process of bone filling, alignment, and ROI selection. (a) An original MD-CT image slice. (b) Filled-in bone. (c) Initial location of distal tibial end plateau (white dot) and the shaded region used for bone alignment. (d) Final ROI covering 12-16% of tibia.
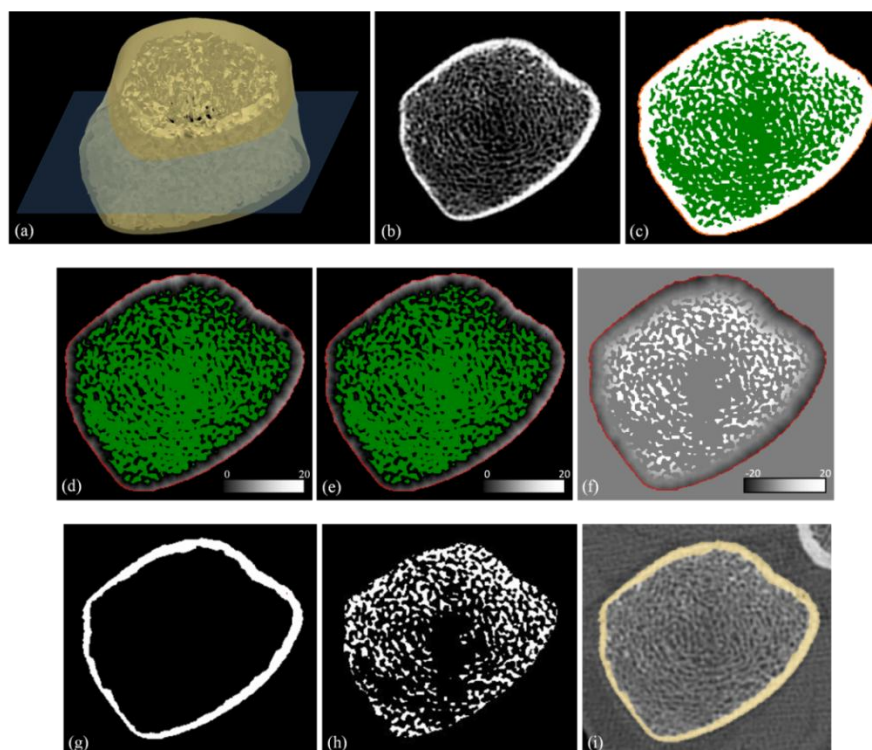
Figure 3   Results of intermediate steps of the cortical bone segmentation algorithm. (a) ROI volume and an image slice used for illustration. (b) BMD image. (c) Marrow space (green), possible cortical pores (blue), and periosteal surface (red). (d) FDT from marrow space and possible cortical pores. (e) Same as (d) after filling confirmed cortical pores. (f) FDT from periosteal boundary by initializing the negative value of local cortical bone thickness; see text for explanation. (g) Cortical bone segmented as the region with negative FDT values in (f). (h) Segmented trabecular bone region. (i) Overlaid cortical bone region on the CT image.

3.2 Cortical Bone Segmentation Algorithm

First, a simple threshold at 1180mg/cc is applied on the BMD image to isolate the bone region from marrow, cortical pores, and the space outside the tibia. Let S_{tibia} denote the set of voxels falling inside the filled-in tibia bone within the target axial cylindrical ROI (Figure 3 (a)) and let f_{BMD} denote the BMD map. Also, let $S_{\text{bone}} \subset S_{\text{tibia}}$ denote the set of bone voxels while $S_{\text{non bone}} = S_{\text{tibia}} - S_{\text{bone}}$ be the set marrow and cortical pore voxels (Figure 3 (c)). Let $S_{\text{periosteum}}$ denote the set of voxels 26-adjacent to S_{tibia}; thus the set of voxels $S_{\text{periosteum}}$ (Figure 3 (c)) wraps around the filled-in tibia bone over the ROI used for cortical bone analyses. The set of voxels outside $S_{\text{tibia}} \cup S_{\text{periosteum}}$, denoted by $S_{\text{background}}$, are excluded. Non-bone voxels $S_{\text{non bone}} \subset S_{\text{tibia}}$ inside the tibia are further classified into confident marrow (green) and possible cortical pore (blue) voxels; let S_{marrow} and S_{pore} denote these two sets. The set S_{marrow} is defined as the largest 6-component of $S_{\text{non bone}}$ and $S_{\text{pore}} = S_{\text{non bone}} - S_{\text{marrow}}$.

The key idea of the segmentation algorithm is to compute cortical bone thickness at every voxel on the periosteal boundary as its distance from the endosteum and then delineate the cortex as the set of all voxels whose distance from some periosteal voxel is smaller than or equal to its thickness value. A major challenge is the presence of cortical pores artificially reducing local thickness at nearby periosteal voxels. Such artifacts are detected by identifying sudden recessions in thickness values along periosteum and then linking those with possible pores. Initial thickness values at periosteal voxels are computed as their FDT values from the set of marrow or possible pore voxels, i.e., $S_{\text{marrow}} \cup S_{\text{pore}}$. For FDT computation during this step, zero value is initialized inside $S_{\text{marrow}} \cup S_{\text{pore}}$ while a large value is initialized inside $S_{\text{bone}} \cup S_{\text{periosteum}}$; finally, the set of voxels $S_{\text{background}}$ is excluded from path propagation. However, as it has already been stated, computed thickness values along the periosteal border may contain sudden recession points due to the presence of cortical pores. On a given slice, a periosteal boundary is a digital 4-closed curve, say, $p_0, p_1, \cdots, p_{i-1}, p_i, p_{i+1}, \cdots, p_{N-1}$. A given

voxel p_i on the periosteum is a *recession voxel* if $FDT(p_i)$ is smaller than half of the average FDT value of the voxels $p_{i\pm j \bmod N}$, where $j = L, L + 1, \cdots, H$. After a recession voxel p_i is detected, the non-bone voxel, say q, nearest to p_i is identified. Finally, if q is a possible pore voxel, i.e., $q \in S_{\text{pore}}$, then the 6-component C_q of S_{pore} containing q is conformed as a cortical pore. Finally, $S_{\text{non bone}}$ is reduced to $S_{\text{non bone}} - C_q$ while S_{bone} is augmented to $S_{\text{bone}} \cup C_q$. After all recession voxels are identified and the pores are filled, the FDT for periosteal thickness is recomputed and the process continues until no new recession voxels are found on periosteum. The iteration will converge in no more than three times during all our experiments due to small amount of pores.

At every voxel $p \in S_{\text{periosteum}}$, the FDT value computed as above gives the cortical bone thickness at p; let us denote it as $\tau(p)$. The purpose of the current and final step of cortical bone segmentation is to delineate the cortical region. The principle of this step is to find the cortex as the set of all voxels whose distance from some periosteal voxel p is less than its cortical thickness $\tau(p)$. This step is accomplished using a modified FDT computation from the periosteum. Specifically, during this step, at each voxel $p \in S_{\text{periosteum}}$, the FDT value is initialized as $-\tau(p)$, the negative of the cortical bone thickness at p. A large value is initialized at each voxel inside S_{bone}; finally, all voxels outside $S_{\text{bone}} \cup S_{\text{periosteum}}$ are excluded for path propagation. Let $\rho(p)$ denote the computed FDT value at each voxel inside S_{bone}. The cortical bone region S_{cortex} is delineated as the set of all bone voxels p with a negative FDT value $\rho(p)$ as follow:

$$S_{\text{cortex}} = \{p \mid p \in S_{\text{bone}} \wedge \rho(p) < 0\}.$$

Finally, the outer layer on cortex is defined as the set of cortex bone voxels which are 6-adjacent to $S_{\text{periosteum}}$; let $S_{\text{outer cortex}}$ denote the outer layer of cortex.
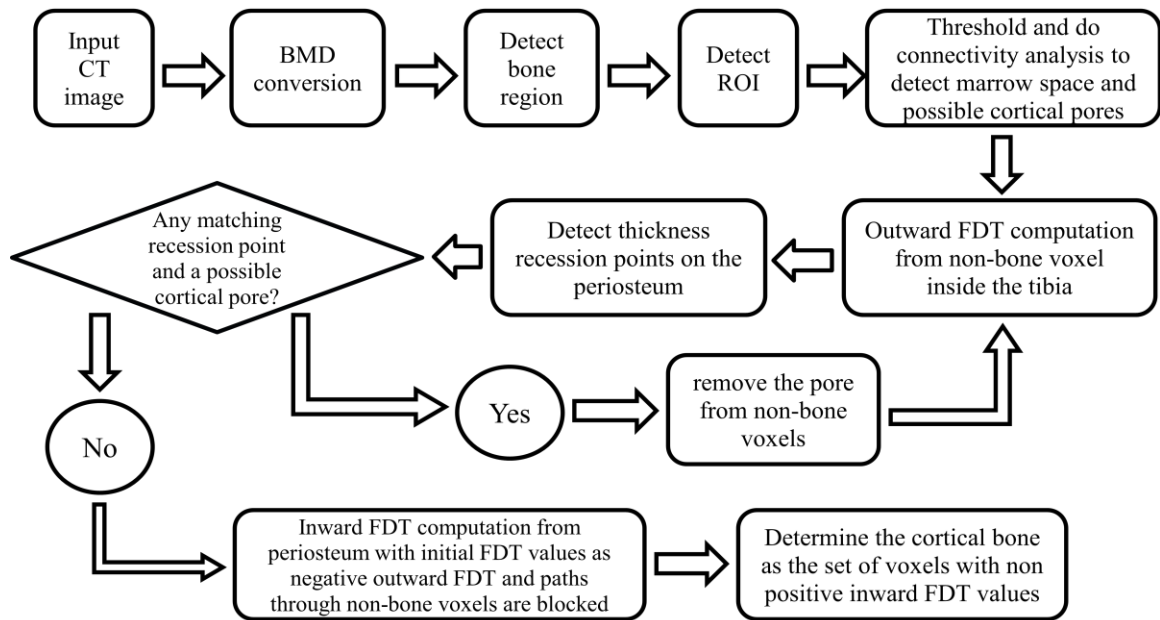
Figure 4   Flow chart indicating major preprocessing tasks and cortical segmentation steps.

3.3 Experimental methods

The aim of our experiments was – (1) to evaluate the method's accuracy in terms of agreement with a gold standard cortical bone segmentation, (2) to examine the method's repeat MD-CT scan reproducibility, and (3) to assess the method's ability to differentiate cortical bone measures among age and height order matched male and female volunteers through *in vivo* MD-CT imaging, and athletes and common people volunteers. All experiments were performed at the distal tibia site. To evaluate the method's accuracy and reproducibility, three repeat scan MD-CT imaging were performed on human cadaveric ankle specimens.

3.3.1   Image processing and analysis

Each image data set was processed through the following cascade of steps – (1) computation of BMD image, (2) bone reorientation, interpolation, and ROI selection, and (3) application of cortical segmentation and analyses on the ROI data. For cadaveric ankle specimens, INTableTM calibration phantom was used to convert the MD-CT

Hounsfield numbers into BMD (mg/cm3) measures while GammaxTM calibration phantom was used for in vivo scans. As described in Section 2.1, four axial cylindrical sections covering 8-16% of tibia were used. Since difference in cortical measures have been found between anterior, posterior, medial and lateral part of bone in previous researches [6][38], each cylindrical section was further subdivided into four angular sections, each covering an angular space of 90° as shown in Figure 5. The line joining the center of gravities of the tibia and the fibula was used as the reference line and the angular space of 360° was divided into four equal angular compartment. Thus, with each of the 4 cylindrical sections being divided into 4 angular regions, altogether 16 ROIs were used for computing cortical bone measures. The cortical bone segmentation algorithm of Section 2.2 was applied on each MD-CT image and cortical thickness and porosity is calculated.

The cortical thickness is calculated as the ratio of ROI cortex volume and ROI cortex surface area, as following:

$$cortical\ thickness = \frac{|S_{cortex}|}{|S_{outer\ cortex}|}$$

Since small pores of cortex are heavily blurred in MD-CT images, traditional method to calculate porosity by pore volume divided by whole cortex volume is easy to fail as giving a result slightly larger than zero. Considering the fact that image voxels are blurred by both bone cortex and marrow, we define porosity which satisfies: $(1 - p) \times \rho_C + p \times \rho_M = \rho_{ad}$, where p is the porosity, ρ_C is the true tissue density of cortex, ρ_M is the true tissue density of marrow, and ρ_{ad} is apparent density of bone, which can be considered as equal to BMD value in MD-CT image. Thus we calculate porosity by:

$$porosity = 1 - \frac{\sum_{p \in S_{\text{cortex}}} BMD(p)}{BMD_{\text{cortical bone}} \times |S_{\text{cortex}}|}$$

Within the range of ROI, ρ_C and ρ_M can be treated as constants. From [39], we can derive $\rho_C = 2184 g/cm^3$ by using ash fraction of cortex as 0.6, and $\rho_M = 900 g/cm^3$.
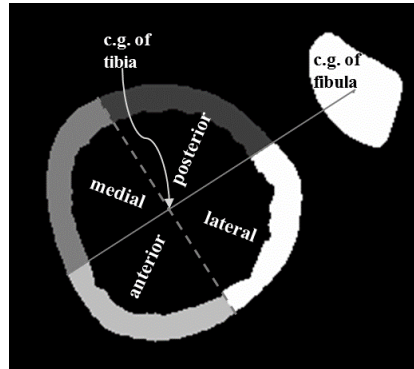
Figure 5   Illustration of angular ROIs using the reference line joining the center of gravity of tibia with that of fibula. Each angular section covers 90º of angular space.

3.3.2   MD-CT Data Acquisition

Twenty-four fresh-frozen human cadaveric ankle specimens were obtained from fourteen body donors (age: 55Y to 91Y). Exclusion criteria for this study were evidence of previous fracture or knowledge of bone tumor or bone metastasis. These ankle specimens were collected under the Deeded Bodies Program, The University of Iowa, Iowa City and were kept frozen until the performance of MD-CT imaging. Forty-five male (M) and fifty-four female (F) volunteers of age between 18 to 23 years were recruited for the in vivo study.

3.3.3   MD-CT Imaging

High resolution MD-CT scans of the distal tibia were acquired at the University of Iowa Comprehensive Lung Imaging Center on a 128 slice SOMATOM Definition Flash scanner (Siemens, Munich, Germany) using the following CT parameters: single tube spiral acquisition at 120kV, 200 effective mAs, pitch factor: 1.0, scan length of

10cm beginning at the distal tibia end-plateau and total effective dose equivalent: 17mrem $\approx$ 20 days of environmental radiation. One AP scout scan of the entire tibia was acquired to locate the field of view (FOV) and to determine tibial length. After scanning each specimen in a helical mode with a 0.4 mm slice thickness, data were reconstructed at 0.2 mm slice thickness using a normal cone beam method with a special U70u kernel achieving high structural resolution. Three repeat MD-CT scans of each distal tibia specimen were acquired after repositioning the specimen on the CT table before each scan.

CHAPTER FOUR

RESULT AND DISCUSSION

4.1　Results

4.1.1　Accuracy of cortical bone segmentation

The experiment for accuracy evaluation of the method was performed on sixteen volunteer tibia *in vivo* scan images. Half of those images were from male volunteers while the other half were from female. To examine the accuracy of MD-CT based cortical bone segmentation, a gold standard segmentation of cortical bone was derived by manually outlining cortical region on twenty MD-CT image slices, among which five consecutive slices were randomly selected from each of the four cylinder ROI sections. Since segmentation of periosteum is region growing with no challenge, and manual drawing is difficult to work as precise as region growing, it means little to manually draw the periosteum. So we only manually drew endosteum and combine it with periosteum to generate the ground truth mask. This work is done by an independent expert using ITK-SNAP software. Let $S_{\text{cortex}}^{\text{true}}$ be the set of voxels falling inside the true cortical bone regions and let $S_{\text{cortex}}^{\text{MD-CT}}$ be computerized segmentation results. Jaccard similarity coefficient (also known as Jaccard index) is used to characterize the accuracy, i.e.,

$$accuracy = \frac{S_{\text{cortex}}^{\text{true}} \cap S_{\text{cortex}}^{\text{MD-CT}}}{S_{\text{cortex}}^{\text{true}} \cup S_{\text{cortex}}^{\text{MD-CT}}}.$$

A quantitative comparison between the manual and computerized segmentation of cortical bone on ten cadaveric ankle images resulted the average accuracy of the 0.951 with a standard deviation of 0.010. Considering challenges of cortical bone segmentation and relatively low resolution offered by MD-CT imaging, and comparing with linear

regression slope of cortical total volume 0.864 reported in [22] (for human data), and dice coefficient (DC) 0.904 reported in [27], the observed accuracy results are encouraging.

4.1.2 Repeat scan reproducibility of cortical bone segmentation

For this experiment, three repositioned repeat scan MD-CT images of twenty-four cadaveric ankle specimens were used. BMD computation, ROIs selection as well as cortical bone segmentation and measurements were performed independently on each repeat scan data. For quantitative assessment of reproducibility of cortical bone segmentation algorithm, repeat scan intra-class correlation (ICC) values were computed for each measure over each ROI from three repeat scan data of twenty-four cadaveric specimens. The observed ICC values for both cortical thickness and porosity measures were high with the average ICC value for cortical thickness over the eight different ROIs being 98.0% $\pm$ 1.4% (mean $\pm$ std.) while that for cortical porosity was 97.9% $\pm$ 0.9% (mean $\pm$ std.). The observed results of for repeat scan reproducibility of cortical bone measures were highly satisfactory confirming the repeatability of cortical bone segmentation and measures.

4.1.3 Results of In Vivo Study

To evaluate the effectiveness of the method, firstly, *in vivo* MD-CT data from forty-five male and fifty-four female volunteers were acquired. Among all female data, forty-five were randomly selected (by MATLAB function *randperm*) to form age similar and height order matched pairs of two genders. The heights of used data are 180.88 $\pm$ 7.89cm (mean $\pm$ std.) for male, and 165.56 $\pm$ 5.62cm (mean $\pm$ std.) for female, and R^2 for two groups of height is 0.972. The cortical bone segmentation and measurement were performed on each image data and a paired t-test was performed for both cortical thickness and porosity measures derived from each of the sixteen ROIs. Quantitative results have shown that male subjects on average have 16.3% thicker cortex and 4.7%

increased porosity as compared to females. Results of pair t-test showed the difference was statistically significant with p-values less than 0.01 on all sixteen ROIs, for both thickness and porosity.

Secondly, *in vivo* MD-CT data from ten athlete volunteers (seven male and three female) were processed. From previous ninety-nine data, ten data which have same gender and the most approximate height were selected to form the control group. The heights are 182.71 ± 6.82cm (mean $\pm$ std.) for athlete, and 182.62 ± 6.77cm (mean $\pm$ std.) for control group, and R^2 for two groups of height is 0.989. Same processes were performed to get cortical thickness and porosity measures on each of the sixteen ROIs. No obvious regional difference for cortical bone thickness is found, with only two ROIs out of sixteen had found p-value less than 0.05. But for cortical porosity, twelve ROIs were found statistically significant with p-values less than 0.05. Quantitative results showed that athlete subjects on average have 3.9% less porosity as compared to control group.

4.2   Discussion

A new automatic method has been developed for cortical bone segmentation. The method has been applied on 3D MD-CT image data of tibia bones. Cortical bone has been successfully segmented. Reproducibility, accuracy and effectiveness of the method have all been well evaluated.

As one parameter, the selection of threshold is important. We hope the threshold will eliminate all marrow while keep all cortical part, and this is usually quite easy to realize during our experiment. Part of the trabecular may remain after doing threshold, and the most important part of our segmentation method is to find the border between the remaining trabecular part and the cortical. Also a suitable threshold can eliminate the blurred region near the boundary of solid bone and soft tissue, which is caused by CT scanner algorithm.

The accuracy of our method is evaluated based on the ground truth generate by manual drawing. In fact, MD-CT image itself has limited resolution to fully showing the details of material comparing with high quality imaging technique such as Micro-CT. So our method on MD-CT may not be as high as segmentation applied methods on Micro-CT. But based on the info human can acquire from MD-CT images, our method is good enough to be applied to get accurate cortical segmentation and measures.

The effectiveness validation of our method shows its potential to be applied in clinical researches. Besides cortical measures in whole cortical region, the longitudinal and angular division of cortical in this paper also provides a method of study cortical properties in different but meaningful regions. The study of athlete bones may lead many new topics about how athletes' training or living style can improve the bone quality.

CHAPTER FIVE

CONCLUSION

A new cortical bone segmentation method along with computation of regional cortical measures has been developed for in vivo MD-CT imaging at a peripheral site. The method is fully automatic and has been successfully applied on cadaveric as well as on *in vivo* MD-CT images of distal tibia. The new cortical bone segmentation method has successfully utilized larger contextual and topologic information of the distal tibial bone geometry. In this context, a new variation of fuzzy thickness computation has been introduced and its application to cortical bone segmentation has been demonstrated. Experimental results on twenty-four cadaveric distal tibia MD-CT data have demonstrated that the method is highly accurate and reproducible. Also, *in vivo* data from age similar and height order matched male and female volunteers has shown that male subjects have thicker and more porous cortex at distal tibia as compared to females, and *in vivo* data from age similar and height order matched athlete volunteers and common people has shown that athletes have less porous cortex at distal tibia.

REFERENCES

[1] Kirmani S., Christen D., van Lenthe G. H., Fischer P. R., Bouxsein M. L., McCready L. K., Melton L. J. 3rd, Riggs B. L., Amin S., Müller R., Khosla S., Bone structure at the distal radius during adolescent growth. J Bone Miner Res. 2009 Jun; 24 (6):1033-42.

[2] Ammann P, Rizzoli R. Bone strength and its determinants. Osteoporos Int. 2003; 14: S13–18.

[3] Seeman E, Delmas PD. Bone quality: the material and structural basis of bone strength and fragility. N Engl J Med. 2006; 354: 2250–2261.

[4] Barck K. H., Lee W. P., Diehl L. J., Ross J., Gribling P., Zhang Y., Nguyen K., van Bruggen N., Hurst S., Carano R. A., Quantification of cortical bone loss and repair for therapeutic evaluation in collagen-induced arthritis, by micro–computed tomography and automated image analysis. Arthritis & Rheumatism, Vol. 50, No. 10, October 2004, pp 3377–3386.

[5] Nishiyama K. K., Macdonald H. M., Buie H. R., Hanley D. A., Boyd S. K., Postmenopausal women with osteopenia have higher cortical porosity and thinner cortices at the distal radius and tibia than women with normal aBMD: an in vivo HR-pQCT Study. Journal of Bone and Mineral Research, Vol. 25, No. 4, April 2010, pp 882–890.

[6] Burghardt A. J., Kazakia G. J., Sode M., A longitudinal HR-pQCT study of alendronate treatment in postmenopausal women with low bone density: relations among density, cortical and trabecular microarchitecture, biomechanics, and bone turnover. Journal of Bone and Mineral Research, Vol. 25, No. 12, December 2010, pp 2558–2571.

[7] Burghardt A. J., Kazakia G. J., Ramachandran S., Link T. M., Majumdar S., Age- and gender-related differences in the geometric properties and biomechanical significance of intracortical porosity in the distal radius and tibia. Journal of Bone and Mineral Research, Vol. 25, No. 5, May 2010, pp 983–993.

[8] Sheu Y, Cauley J. A., Bunker C. H., Wheeler V. W., Patrick A. L., Gordon C. L., Kammerer C. M., Zmuda J. M., Correlates of trabecular and cortical volumetric BMD in men of african ancestry. Journal of Bone and Mineral Research, Vol. 24, No. 12, May 2009, pp 1960-1968.

[9] Walker M. D., Liu X. S., Stein E., Zhou B., Bezati E., McMahon D. J., Udesky J., Liu G., Shane E., Guo X. E., Bilezikian J. P., Differences in bone microarchitecture between postmenopausal Chinese-American and white women. Journal of Bone and Mineral Research, Vol. 26, No. 7, July 2011, pp 1392–1398.

[10] Seeman E., Delmas P. D., Hanley D. A., Sellmeyer D., Cheung A. M., Shane E., Kearns A., Thomas T., Boyd S. K., Boutroy S., Bogado C., Majumdar S., Fan M., Libanati C., Zanchetta J., Microarchitectural deterioration of cortical and trabecular bone: differing effects of denosumab and alendronate. Journal of Bone and Mineral Research, Vol. 25, No. 8, August 2010, pp 1886–1894.

[11] Zanchetta J. R., Bogado C. E., Ferretti J. L., Wang O., Wilson M. G., Sato M., Gaich G. A., Dalsky G. P., Myers S.L., Effects of teriparatide [recombinant human parathyroid hormone (1-34)] on cortical bone in postmenopausal women with osteoporosis. Journal of Bone and Mineral Research, Vol. 18, No. 3, 2003, pp539-543.

[12] Wachter N. J., Krischak G. D., Mentzel M., Sarkar M. R., Ebinger T., Kinzl L., Claes L., Augat P., Correlation of bone mineral density with strength and microstructural parameters of cortical bone in vitro. Bone, Vol. 31, No. 1, July 2002:90–95.

[13] MacNeil J. A., Boyd S. K., Load distribution and the predictive power of morphological indices in the distal radius and tibia by high resolution peripheral quantitative computed tomography. Bone 2007; 41: 129–37.

[14] Boutroy S., van Rietbergen B., Sornay-Rendu E., Munoz F., Bouxsein M. L., Delmas P. D., Finite element analysis based on in vivo HR-pQCT images of the distal radius is associated with wrist fracture in postmenopausal women. J Bone Miner Res 2008; 23: 392–9.

[15] Melton III L. J., Riggs B. L., van Lenthe G. H., Achenbach SJ, Muller R, Bouxsein ML, Amin S., Atkinson E. J., Khosla S., Contribution of in vivo structural measurements and load/strength ratios to the determination of forearm fracture risk in postmenopausal women. J Bone Miner Res 2007; 22: 1442–8.

[16] Bae W. C., Chen P. C., Chung C. B., Masuda K, D'Lima D, Du J., Quantitative Ultrashort Echo Time (UTE) MRI of human cortical bone: correlation with porosity and biomechanical properties. Journal of Bone and Mineral Research, Vol. 27, No. 4, April 2012, pp 848–857.

[17] Saha P. K., Gomberg B. R., and Wehrli F. W., Three-dimensional digital topological characterization of cancellous bone architecture. International Journal of Imaging Systems and Technology, vol. 11, pp. 81-90, 2000.

[18] Wehrli F. W., Saha P. K., Gomberg B. R., Song H. K., Snyder P. J., Benito M., Wright A., and Weening R., Role of magnetic resonance for assessing structure and function of trabecular bone. Topics in Magnetic Resonance Imaging, vol. 13, pp. 335-356, 2002.

[19] Saha P. K, Wald M. J., Radin A., predicting mechanical competence of trabecular bone using 3D tensor-scale based parameters. Medical Imaging 2005: Physiology, Function, and Structure from Medical Images, Volume 5746, 2005, pp. 279-290.

[20] Rüegsegger P, Koller B, Müller R. A microtomographic system for the nondestructive evaluation of bone architecture. Calcif Tissue Int Jan 1996; 58(1):24–9.

[21] Barck K., Lee W., Diehl L., Ross J., Gribling P., Zhang Y., Nguyen K., Bruggen N., Hurst S., Carano R., Quantification of cortical bone loss and repair for therapeutic evaluation in collagen-induced arthritis, by micro–computed tomography and automated image analysis. Arthritis & Rheumatism, Volume 50, Issue 10, pages 3377–3386, October 2004.

[22] Helen R. Buie, Graeme M. Campbell, R. Joshua Klinck, MacNeil J. A., Boyd S. K., Automatic segmentation of cortical and trabecular compartments based on a dual threshold technique for in vivo micro-CT bone analysis. Bone 41 (2007) 505–515.

[23] Laib A, Häuselmann HJ, Rüegsegger P., In vivo high resolution 3D-QCT of the human forearm. Technol Health Care Dec 1998; 6 (5–6):329–37.

[24] Kass M, Witkin A, Terzopoulos D., Snakes: active contour models. Int. J Comput Vis 1988; 1 (4):321–31.

[25] Gelaude F, Vander SJ, Lauwers B., Semi-automated segmentation and visualisation of outer bone cortex from medical images. Comput Methods Biomech Biomed Engin Feb 2006; 9 (1):65–77.

[26] Gomberg B. R., Saha P. K, Wehrli F. W., method for cortical bone structural analysis from magnetic resonance images. Acad Radiol 2005; 12:1320–1332.

[27] Valentinitsch A., Patsch J.M., Deutschmann J., Schueller-Weidekamm C., Resch H., Kainberger F., Langs G., Automated threshold-independent cortex segmentation by 3D-texture analysis of HR-pQCT scans. Bone 51 (2012) 480–487.

[28] Treece G.M., Gee A.H., Mayhew P.M., Poole K.E.S., High resolution cortical bone thickness measurement from clinical CT data. Medical Image Analysis 14 (2010) 276–290.

[29] Treece G.M., Poole K.E.S., Gee A.H., Imaging the femoral cortex: Thickness, density and mass from clinical CT. Medical Image Analysis 16 (2012) 952–965.

[30] Udupa J. K. and Samarasekera S., Fuzzy Connectedness and Object Definition: Theory, Algorithms, and Applications in Image Segmentation. Graphical Models and Image Processing, Vol. 58, No. 3, May, pp. 246–261, 1996, Article No. 0021.

[31] Udupa J. K., and Saha P. K., Fuzzy Connectedness and Image Segmentation. Proceedings of The IEEE, VOL. 91, NO. 10, October 2003.

[32] Sonka M., Hlavac V., Boyle R., Image Processing: Analysis and Machine Vision, 3rd version. ISBN10: 0-495-08252-X, Thomson Corporation, 2008.

[33] Saha P. K. and Udupa J. K., Relative fuzzy connectedness among multiple objects: theory, algorithms, and applications in image segmentation. Computer Vision and Image Understanding, 82:42-56, 2000a.

[34] Saha P. K. and Udupa J. K., Scale-based fuzzy connectivity: a novel image segmentation methodology and its validation. In SPIE Conference on Image Processing, San Diego, California, pages 246-257, 2 1999.

[35] Saha P. K. and Udupa J. K. Iterative relative fuzzy connectedness and object definition: theory, algorithms, and applications in image segmentation. In Proceedings of the IEEE Workshop on Mathematical Methods in Biomedical Image Analysis (MMBIA '00), pages 254-269, 2000b.

[36] Saha P. K, Wehrli F. W., Gomberg B. R., Fuzzy distance transform: theory, algorithms, and applications. Computer Vision and Image Understanding 86, 171–190 (2002).

[37] Saha P. K, Wehrli F. W., Measurement of trabecular bone thickness in the limited resolution regime of in vivo MRI by fuzzy distance transform. IEEE Transactions on Medical Imaging, VOL. 23, NO. 1, January 2004.

[38] Lai Y. M., Qin L., Hung V. W., and Chan K. M., Regional differences in cortical bone mineral density in the weight-bearing long bone shaft--a pQCT study. Bone. 36, 465-471 (2005).

[39] Hernandez C. J., Beaupré G. S., Keller T. S., and Carter D. R., The influence of bone volume fraction and ash fraction on bone strength and modulus. Bone. 29, 74-78 (2001).